Guo *et al. Energy Mater.* **2025**, *5*, 500098
DOI: 10.20517/energymater.2024.305

Energy Materials

Article

Open Access

A quantitative reconstruction strategy for the surface structure of $LiNi_{0.80}Co_{0.15}Al_{0.05}O_2$ cathode material

Xingbo Guo[1], Junli Yang[1], Guixian Deng[1], Xinfang Cao[1], Bo Zhang[2,*], Tao Deng[2], Yong Zhu[3], Jianbo Liu[3], Wenzhang Wang[3], Shubiao Xia[1,*]

[1]Yunnan Key Laboratory of Crystalline Porous Organic Functional Materials, College of Chemistry and Materials Engineering, Qujing Normal University, Qujing 655011, Yunnan, China.
[2]Guiyang Industrial Technology Research Institute, Guiyang Vocational and Technical College, Guiyang 550081, Guizhou, China.
[3]Guizhou Anda Technology Energy Co., Ltd, Guiyang 550000, Guizhou, China.

Correspondence to: Dr. Bo Zhang, Guiyang Industrial Technology Research Institute, Guiyang Vocational and Technical College, 3 Yuntan South Road, Guanshanhu District, Guiyang 550081, Guizhou, China. E-mail: 17820125peng@shu.edu.cn; Prof. Shubiao Xia, Yunnan Key Laboratory of Crystalline Porous Organic Functional Materials, College of Chemistry and Materials Engineering, Qujing Normal University, 222 Sanjiang Avenue, Qilin District, Qujing 655011, Yunnan, China. E-mail: xiashubiao@mail.qjnu.edu.cn

How to cite this article: Guo, X.; Yang, J.; Deng, G.; Cao, X.; Zhang, B.; Deng, T.; Zhu, Y.; Liu, J.; Wang, W.; Xia, S. A quantitative reconstruction strategy for the surface structure of $LiNi_{0.80}Co_{0.15}Al_{0.05}O_2$ cathode material. *Energy Mater.* **2025**, *5*, 500098. https://dx.doi.org/10.20517/energymater.2024.305

Received: 26 Dec 2024 **First Decision:** 5 Feb 2025 **Revised:** 11 Mar 2025 **Accepted:** 27 Mar 2025 **Published:** 9 May 2025

Academic Editor: Jiazhao Wang **Copy Editor:** Fangling Lan **Production Editor:** Fangling Lan

Abstract

To address the detrimental impact of residual LiOH on the electrochemical performance of $LiNi_{0.80}Co_{0.15}Al_{0.05}O_2$ (NCA) cathode material, it is imperative to optimize its surface structure. Adding a Li-reactant to react with residual LiOH on the cathode surface not only removes residual LiOH but also forms new surface structure layers. However, this reaction process not only necessitates evaluating the compatibility between the newly formed surface layer and the crystal structure of the NCA cathode material but also requires careful determination of the optimal amount of Li-reactant. Currently, there remains a lack of well-established theoretical guidance for determining the optimal addition amount of lithium reactants. In this study, the quantitative addition of 6,000 ppm Al_2O_3 as a Li-reactant to react with the residual 3,156 ppm LiOH on the NCA surface not only effectively reduces the residual LiOH but also facilitates the formation of a $LiAlO_2$@NCA heterostructure on the NCA cathode materials. This approach provides a theoretical foundation for the addition of Li-reactant, overcomes the limitations of empirical trial-and-error methods, and achieves quantitative reconstruction of the NCA cathode materials surface structure. Based on an in-depth analysis of the surface structure, first-principles calculations and

electrochemical performance tests, the $LiAlO_2$@NCA heterostructure not only serves as an efficient Li^+ diffusion channel and reduces the Li^+ migration energy barrier, but also provides a stable protection of the surface of the cathode material, thereby enhancing its stability and reversibility.

Keywords: Quantitative reconstruction, residual LiOH, Al_2O_3, heterostructure

INTRODUCTION

To achieve the goal of carbon neutrality by 2050, reducing carbon emissions necessitates a coordinated effort. Expanding the market share of electric vehicles is one of the most effective measures[1]. However, electric vehicles still face several challenges, including driving range, safety, and cost. These issues primarily stem from the power source and key components of electric vehicles - lithium-ion batteries[2]. Among these components, the cathode and anode materials are crucial to lithium-ion batteries, as they directly influence the capacity and stability of the lithium-ion batteries. A wide range of novel anode materials has emerged, exhibiting not only high capacity but also exceptional cycle stability[3-6]. The cathode material has emerged as the primary factor limiting the performance of lithium-ion batteries. Currently, numerous researchers are focused on developing cathode materials that possess high energy density, extended cycle life, and reduced cost[7-9]. NCA cathode materials have garnered significant attention from researchers and battery manufacturers owing to their superior electrochemical properties[10]. However, the application of NCA cathode materials continues to face challenges, including rapid capacity decay, structural instability, and safety concerns.

Residual lithium compounds are the main culprits for the rapid capacity decay, structural instability and low safety performance of NCA cathode materials[11]. During air exposure, the alkaline NCA cathode surface and residual lithium (Li_2O) form compounds such as LiOH and Li_2CO_3, as given in[12-14]

$$Li_2O + CO_2 \rightarrow Li_2CO_3 \quad (1)$$

$$Li_2O + H_2O \rightarrow 2LiOH \quad (2)$$

During the slurry preparation of cathode materials, lithium-ion deintercalation, and practical application, residual LiOH may pose substantial safety risks[15-17]. During the preparation of electrode materials, residual LiOH can act as an inducer for slurry gelation and flocculation, which hinders the preparation of electrodes[18,19]. During charge-discharge cycles, residual LiOH forms an insulating layer that hinders Li^+ migration and reduces the capacity of the cathode material[20,21]. Residual LiOH reacts with the electrolyte to release CO_2 gas, leading to battery expansion and localized overheating, which significantly reduces the safety performance of the battery[22-24].

To reduce the amount of residual LiOH, researchers are investigating various surface optimization strategies to improve the surface structure and enhance the surface stability of the cathode material. These strategies include washing[25], slurry additives[26], surface coating[27], *etc*. The addition of a surface coating layer is a simple and effective method to reconstruct the surface structure of the cathode material, mitigate the adverse effects caused by residual LiOH on the surface, and enhance the surface stability of the cathode material. Common coating layers include oxides[28], phosphates[29], conductive polymers[30], and other ionic conductors[31]. Among various coatings, Al_2O_3 has become the most representative surface coating material due to its high chemical stability, readily available raw materials and excellent economic performance[32].

Adding a Li-reactant to react with residual lithium compounds on the cathode surface not only removes these compounds but also forms new surface structure layers, such as Li_3PO_4[29], LiF[33], and Li_3BO_3[34]. In previous studies, Al_2O_3 has predominantly been employed as a coating material. The research by Negi *et al.* indicates that Al_2O_3 can also serve as a Li-reactant[35]. Through multiple comparative experiments, Negi *et al.* verified the feasibility of adding 1.00 wt% of alumina to react with the residual lithium compounds and achieved an improvement in cycle stability. Although Negi *et al.* can determine a relatively optimal addition amount through comparative experiments, this approach lacks a clear theoretical foundation and is both time-consuming and resource-intensive[35]. However, another critical issue that cannot be overlooked is the mismatch between the crystal structure of the surface layer and that of the bulk material. During cycling, this lattice mismatch between the cathode material and its surface layer hinders long-term cyclability and can induce micro-cracks propagating from the surface to the interior of the cathode material[36]. It is evident that a simplistic surface optimization strategy is insufficient for enhancing the surface structure and stability of the cathode material. To effectively optimize the surface structure through the addition of Li-reactant, it is essential to consider both the compatibility with the crystal structure of the cathode material and the appropriate amount of Li-reactant added. $LiAlO_2$, as an excellent surface material, has been extensively demonstrated by numerous studies to exhibit a high Li^+ ionic conductivity (3×10^{-5} $\Omega^{-1}cm^{-1}$), a high Li^+ diffusion coefficient (D_{Li}, 2.8×10^{-11} m^2s^{-1}), and remarkable stability under high humidity (40%-50%) and high voltage (> 4.5 V) conditions[32,37-39]. In addition, compared with other coatings, the $LiAlO_2$ not only functions as a fast ion conductor but also exhibits a layered structure similar to that of NCA cathode materials. This indicates that the $LiAlO_2$ structural layer can be well matched with the structure of the NCA cathode materials, thereby preventing the propagation of micro-cracks from the surface layer to the inner layer due to lattice mismatch between the added surface structural layer and the NCA cathode material.

In this study, Al_2O_3 is selected as the Li-reactant, and the residual LiOH content is determined to be 3,156 ppm by potentiometric titration. By quantitatively adding 6,000 ppm Al_2O_3 to transform the residual LiOH, the surface structure is reconstructed, resulting in the formation of a $LiAlO_2$@NCA heterostructure. The process of quantitatively converting the residual LiOH on the surface by precisely adding Al_2O_3 is referred to as quantitative reconstruction. This modification enhances the cyclic stability of the cathode material. The paper provides an in-depth examination of how the $LiAlO_2$@NCA heterostructure affects the interconnections among the crystal structure, surface structure, surface composition, and electrochemical characteristics of the cathode materials.

EXPERIMENTAL SECTION

Materials synthesis

The $Ni_{0.80}Co_{0.15}Al_{0.05}(OH)_2$ precursor powder synthesized via the co-precipitation method was combined with an excess of $LiOH{\cdot}H_2O$ (molar ratio of n_{Li}/n_{TM} = 1.05:1.00) and manually ground for half an hour. Subsequently, the mixture was transferred to a tube furnace and heated under an oxygen atmosphere. First, it was heated from ambient temperature to 450 °C at a rate of 5 °C min^{-1} and maintained at this temperature for 5 h. Then, the temperature was further increased to 750 °C at the same heating rate and held for 12 h. Finally, the sample was cooled down to room temperature to produce the $LiNi_{0.80}Co_{0.15}Al_{0.05}O_2$ cathode material, which was designated as NCA.

Based on the weight ratio of Al_2O_3/NCA = 6,000 ppm, Al_2O_3 powder was incorporated into the NCA cathode material and thoroughly mixed by grinding for 30 min. Subsequently, the mixture was subjected to heat treatment in an oxygen environment, where it was ramped to 500 °C at a rate of 5 °C min^{-1}, maintained at this temperature for 6 h, and finally cooled down to ambient temperature. The resulting material was labeled as NCA-6000. The resultant process is illustrated in Figure 1A.

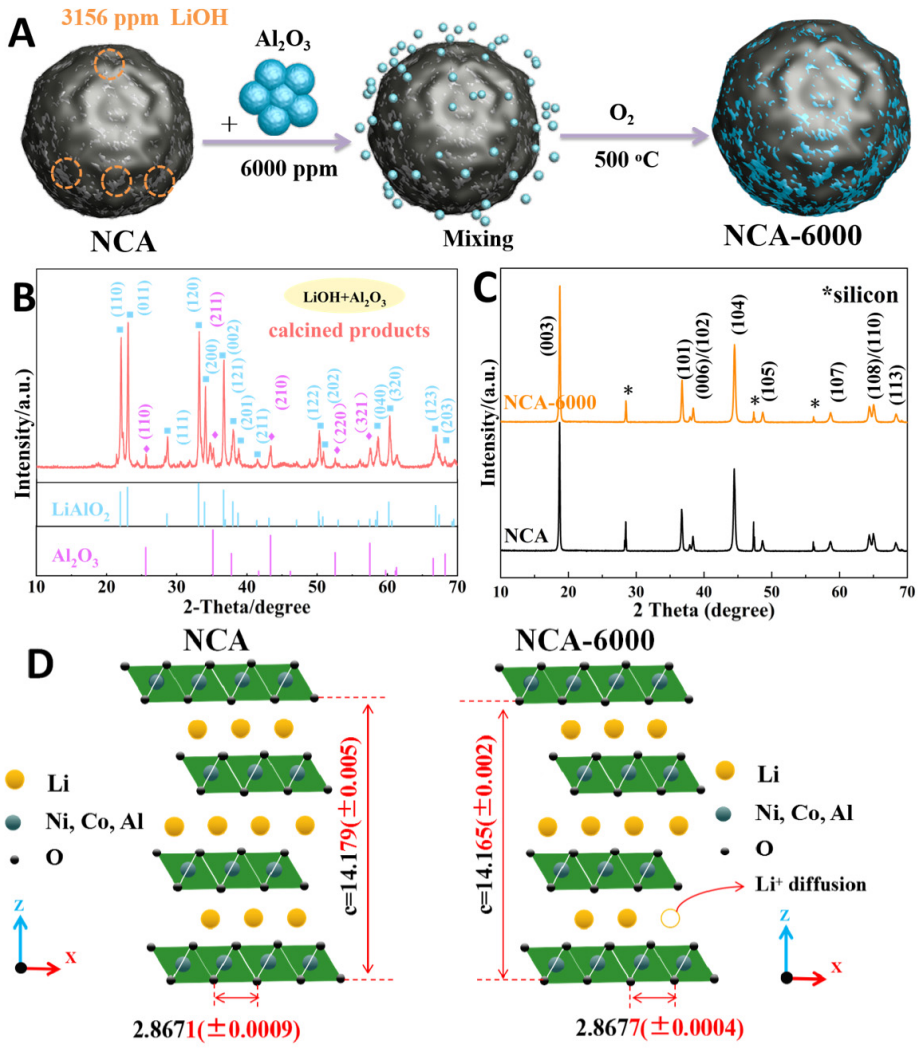

Figure 1. (A) Schematic diagram of surface quantitative reconstruction by adding Al_2O_3; (B)XRD pattern of Al_2O_3 and LiOH calcined products; (C) XRD patterns of NCA and NCA-6000 samples; (B) Schematic diagram of lattice parameter changes in NCA and NCA-6000 samples.

Material characterization

In this study, the crystal structure of the samples was characterized using RIGAKU TTRIII-18KW X-ray diffraction (XRD). The microstructure of secondary particles and the distribution of Ni, Co, and Al elements in NCA and NCA-6000 samples were examined by Nova-Nano450 field emission scanning electron microscopy (SEM) combined with energy dispersive spectroscopy (EDS). The lattice fringes of NCA-6000 samples were further analyzed using Talos F200S high-resolution transmission electron microscopy (HR-TEM) from FEI Company, USA. The valence states of Ni, Al, C, and O elements in NCA and NCA-6000 samples were investigated via PHI5000 X-ray photoelectron spectroscopy (XPS). Additionally, the detailed methodology for determining residual lithium content in NCA and NCA-6000 samples is provided in the Supplementary Materials.

Electrochemical measurements

The cathode material, carbon black, and polyvinylidene fluoride (PVDF) were accurately weighed and uniformly mixed at a mass ratio of 8:1:1. Subsequently, N-methyl-2-pyrrolidone (NMP) was added

dropwise to the mixture, which was then thoroughly stirred to form a homogeneous slurry. The slurry was coated onto aluminum foil using a small-scale coater, followed by vacuum drying, rolling, and cutting to produce the cathode sheet with a loading of 7.06~8.16 mg·cm^{-2} of cathode material. Finally, in an argon-filled glove box, the dried cathode sheet, lithium sheet (as the counter electrode), and separator were assembled into CR2025-type coin cells. The electrolyte used in assembling the battery is 1 M $LiPF_6$ in EC/DMC/EMC (with a volume ratio of 1:1:1). The assembled batteries were evaluated for their initial charge-discharge performance, rate capability, and cycling stability using the LAND-BT2022A battery testing system. Additionally, cyclic voltammetry (CV) measurements at various scan rates and electrochemical impedance spectroscopy (EIS) analyses of batteries in different states (frequency range: 0.01 Hz to 100 kHz) were performed using the PMC-2000A electrochemical workstation.

Computational details

In this study, CASTEP software package was used to optimize $LiAlO_2$, NCA and $LiAlO_2$@NCA respectively. The electron correlation potential is described using the generalized gradient approximation-Perdew-Burke-Ernzerhof (GGA-PBE). The calculations were performed using ultra-soft pseudopotentials, with the following valence electron configurations selected for each element: O: $2s^2 2p^4$, Li: $2s^1$, Ni: $3d^8 4s^2$, Co: $3d^7 4s^2$, Al: $3s^2 3p^1$. In the $LiAlO_2$ and NCA models, the k-point mesh in the Brillouin zone was set to 2 × 2 × 1, and the Brillouin zone integration was performed using the Monkhorst-Pack scheme. Among these parameters, the plane-wave cutoff energy is set to 381.0 eV, the self-consistent convergence accuracy is 1 × 10^{-5} eV atom^{-1}, and the force convergence criterion is 0.03 eV Å^{-1}. The exchange-correlation potential is calculated on a standardized fast Fourier transform grid (45 × 45 × 72).

RESULTS AND DISCUSSION

The surface concentrations of residual LiOH and Li_2CO_3 in the prepared NCA cathode material are measured using potentiometric titration, yielding values of 3,156 and 6,290 ppm, respectively. These results are summarized in Supplementary Table 1. In conjunction with previous studies[40], Al_2O_3 and LiOH can react within a specific temperature range. The reaction for Al_2O_3 and LiOH is presented in (500 °C, $\triangle G$ = -90 kJ mol^{-1}):

$$2LiOH + Al_2O_3 = 2LiAlO_2 + H_2O\ (g) \quad \triangle G < 0\ (0\text{-}500\ ^\circ C) \tag{3}$$

based on which, the product of the reaction between Al_2O_3 and LiOH is $LiAlO_2$.

Therefore, the residual LiOH can be converted into $LiAlO_2$ through the quantitative addition of Al_2O_3. Temperature plays a crucial role in the formation of the $LiAlO_2$ structural layer. If the temperature is too low, it will be insufficient to facilitate the reaction between the added Al_2O_3 and residual LiOH. Conversely, excessively high temperatures will increase production costs. The ΔG values for reaction Equation (3) at various temperatures are detailed in Supplementary Table 2. To verify the feasibility of this quantitative conversion strategy, Al_2O_3 and LiOH are mixed according to the stoichiometric ratio in Equation (3). The resulting mixture is placed in a tube furnace and heated from room temperature to 500 °C at a heating rate of 5 °C min^{-1} under an oxygen atmosphere for 5 h. As illustrated in Figure 1B, the primary product of the calcination reaction between Al_2O_3 and LiOH is $LiAlO_2$. The XRD pattern for the added Al_2O_3 can be found in Supplementary Figure 1. It is evident that quantitatively adding Al_2O_3 to transform the residual LiOH of the cathode material into a layered $LiAlO_2$ surface structure layer is feasible. This approach enables the quantitative reconstruction of the cathode material's surface structure.

According to the measured values of surface residual LiOH and reaction Equation (3), the NCA-6000 sample was prepared by incorporating 6,000 ppm Al_2O_3 to react with the 3,156 ppm residual LiOH present on the surface of the NCA cathode material (Taking precision into account, 3,156 ppm LiOH is approximated to 3,000 ppm. Based on the stoichiometric requirements of reaction (3), an addition of 6,000 ppm Al_2O_3 is necessary to completely react with the 3,000 ppm residual LiOH on the surface). Potentiometric titration reveals that the NCA-6000 samples contain only 1,091 ppm of residual LiOH on their surfaces, demonstrating that the precise addition of Al_2O_3 significantly decreases the level of residual LiOH on the NCA cathode material. Nevertheless, a trace amount of LiOH still persists on the surface. This phenomenon is ascribed to the migration of Li^+ ions from within the cathode material to the particle surface during the reheating process at 500 °C. As the material cools afterward, the migrated Li^+ ions react with CO_2 and H_2O in the ambient air, resulting in the generation of new LiOH and Li_2CO_3 layers on the cathode material's surface.

In Figure 1C, the XRD patterns of the NCA and NCA-6000 samples are presented. Both samples display a highly ordered hexagonal layered α-$NaFeO_2$ structure belonging to the space group $R\bar{3}m$. Two pairs of diffraction peaks (108)/(110) and (006)/(102) split significantly, indicating that both samples have ideal layered structures[41]. This could be due to the relatively low concentrations of both the added Al_2O_3 and the formed $LiAlO_2$. The lattice parameters of the two samples were determined using the Si internal standard method, and the results are summarized in Supplementary Table 1. Compared with NCA, the c-axis lattice parameter of NCA-6000 is slightly reduced. As illustrated in Figure 1D, this can be explained by the diffusion of a minor amount of Li from the core of the cathode material particles to the surface. This process leads to a reduction in the Li^+ content within the Li layer and a slight rise in the occupancy of Ni^{2+} in the same layer(r_{Ni2+} = 0.69, r_{Li+} = 0.76 Å)[32].

The SEM images of the NCA and NCA-6000 samples are shown in Figure 2A-D. It is evident that the secondary particle morphology of both samples shows no remarkable differences, and both consist of nanoscale primary particles with an average size of around 10 nm. However, in the EDS mapping of the NCA-6000 sample [Figure 2E-H], besides the homogeneous distribution of Ni, Co, and Al elements, a slight surface enrichment of Al is also detected. This observation could be associated with the formation of a $LiAlO_2$ structural layer, which arises from the reaction between LiOH and Al_2O_3 on the surface of the cathode material. The surface structure of NCA-6000 samples is further analyzed by TEM. As illustrated in Figure 2I and J and Supplementary Figure 2, the surface structure of the NCA-6000 sample displays a pronounced heterogeneous morphology. Additionally, the development and distribution of the $LiAlO_2$ structural layer are strongly linked to the existence of residual LiOH. Region I displays lattice fringes with a d-spacing of 0.4784 nm, which matches the (003) plane of NCA[42]. In contrast, region II shows distinct lattice fringes that differ from those of NCA, with a spacing of 0.2047 nm corresponding to the (104) plane of $LiAlO_2$ (PDF#44-0224)[43]. Through XRD, SEM, and TEM analyses, it is observed that the added Al_2O_3 reacts with residual LiOH to form a heterostructure layer of $LiAlO_2$@NCA on the surface of the cathode material, enabling quantitative reconstruction of the surface structure of the cathode material.

To investigate the impact of the $LiAlO_2$@NCA heterostructural layer on the structural integrity, stability, and electrochemical performance of the cathode material, the surface structures of $LiAlO_2$, NCA and NCA-6000 are modeled and analyzed, as illustrated in Figure 3. Using the NCA as a matrix, a $LiAlO_2$@NCA heterostructure is formed on its surface. As shown in Figure 3A and B, the band structures of both $LiAlO_2$ (E_g = 5.94 eV) and NCA (E_g = 3.11 eV) reveal wide-bandgap semiconductor characteristics. However, the band structure of the $LiAlO_2$@NCA heterostructures reveals characteristics typical of conductors [Figure 3C]. The electron energy levels of the $LiAlO_2$@NCA heterostructure exhibit unique electrochemical

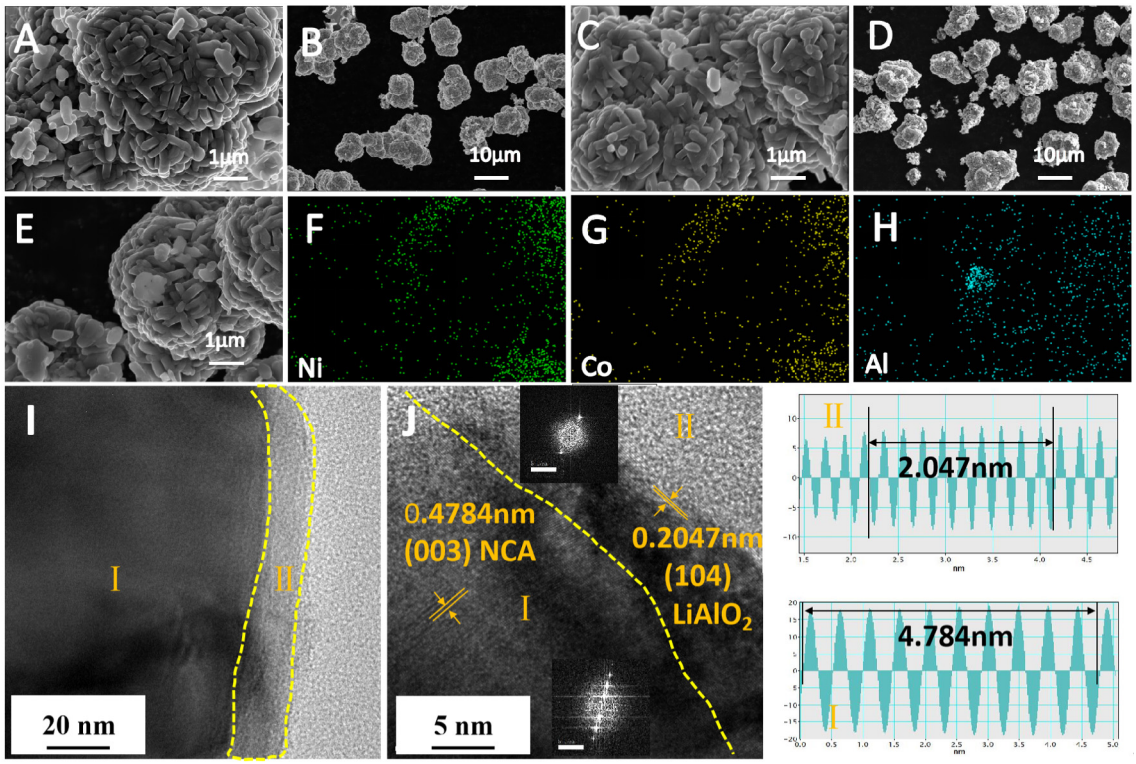

Figure 2. SEM images of NCA and NCA-6000 (A and B) NCA; (C and D) NCA-6000; (E-H) SEM and EDS surface scanning element distribution map of NCA-6000 elements of Ni, Co and Al; (I and J) TEM image of the NCA-6000.

properties and provide excellent electron conductivity. In practical applications, the $LiAlO_2$@NCA heterostructure can effectively enhance current efficiency, reduce the ion migration energy barrier, significantly improve electron polarization during charge/discharge cycles, and boost the rate performance of cathode materials.

To uncover the underlying reasons, the charge density distributions of the two substrates ($LiAlO_2$ and NCA) and atoms are further analyzed. As illustrated in Figure 3D, the valence band top of $LiAlO_2$ is primarily dominated by O-2p orbitals, with a minor contribution from weakly localized Al-3p orbitals. The weak localization of Al-3p allows it to form stable hybrid states with O-2p, effectively suppressing lattice oxygen release. While Al^{3+} does not participate in redox reactions, it stabilizes the oxygen framework, thereby reducing interfacial side reactions. As shown in Figure 3E, the valence band top of NCA is predominantly composed of Ni-3d orbitals, with contributions from Co-3d and O-2p orbitals. The strong localization of the Ni-3d orbitals indicates that their electron cloud distribution is highly concentrated near the atomic nucleus. This localization necessitates overcoming a higher electronic transition energy barrier during the Ni^{2+}/N^{3+} oxidation process, significantly reducing the redox reaction rate. Additionally, the localized Ni-3d orbitals enhance the covalency of the Ni-O bond, thereby restricting lithium-ion migration within the layered structure. Although the Co-3d orbitals also exhibit strong charge localization, their significant energy level splitting facilitates electronic transitions in the Co^{3+}/Co^{4+} redox reaction, partially offsetting the negative effects of localization. Moreover, the hybridization between Co-3d and O-2p orbitals forms delocalized states, accelerating the charge transfer process.

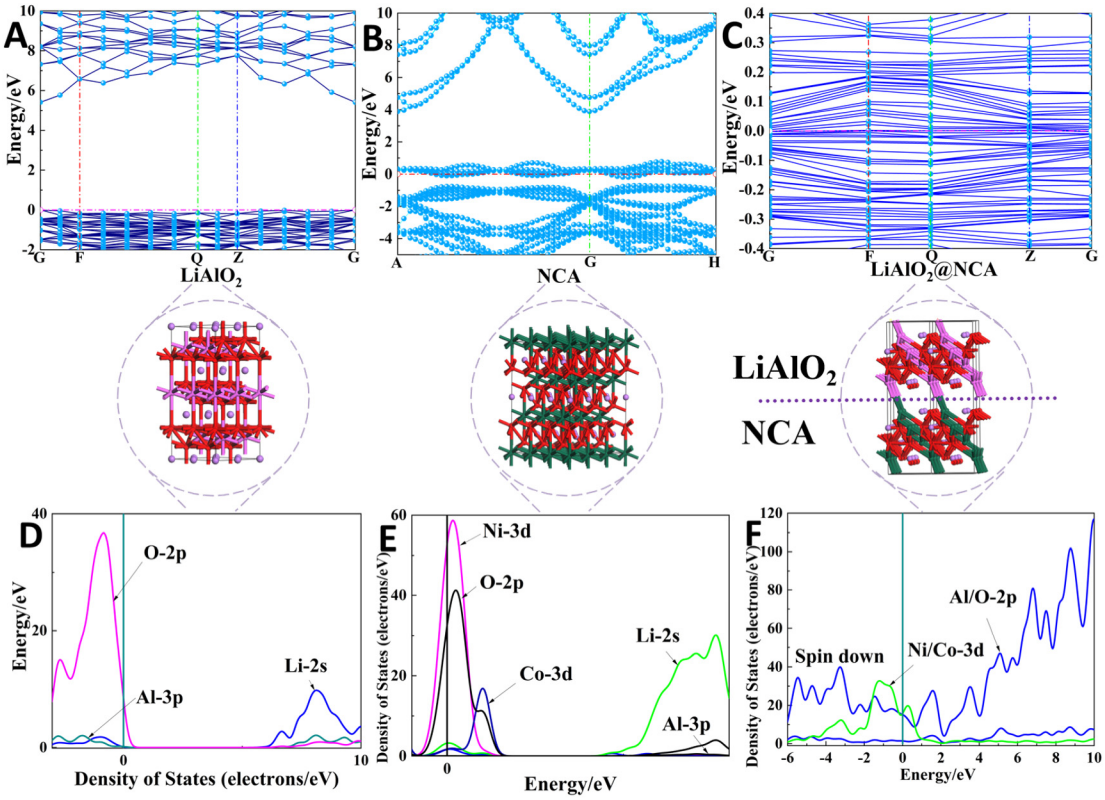

Figure 3. Energy band and structure (A) $LiAlO_2$; (B) NCA; (C) $LiAlO_2$@NCA; State density diagram (D) $LiAlO_2$; (E) NCA; (F) $LiAlO_2$@NCA.

The $LiAlO_2$@NCA heterostructure achieves gradient localized electronic states through orbital hybridization at the interface (Ni-3d/O-2p and Al-3p/O-2p). These interface states bridge the strongly localized Ni-3d and delocalized O-2p orbitals, lowering the charge transfer barrier. Through this interface state regulation, the $LiAlO_2$@NCA heterostructure balances localized and delocalized characteristics, reduces the charge transfer energy barrier, optimizes overall redox kinetics, and achieves a synergistic enhancement in both kinetics and stability.

As shown in Figure 3F, the density of states (DOS) distribution of the $LiAlO_2$@NCA heterostructure is a result of this regulation. The valence bands are primarily formed by the hybridization of Ni-3d, Co-3d, and O-2p orbitals, while the conduction bands are contributed to by the hybridization of O-2p and Al-3p orbitals. Each band exhibits a high degree of localization. The energy loss function also illustrates this point from another perspective. As shown in Supplementary Figure 3, the degree of energy loss caused by charge movement in the $LiAlO_2$@NCA heterostructure is significantly reduced. The formation of the $LiAlO_2$@NCA heterostructure improves the band structure of the original system, introduces interface state characteristics, and enhances electron conductivity.

XPS is further employed to analyze the surface composition of the NCA and NCA-6,000 samples, with the results presented in Figure 4, full spectrum Supplementary Figure 4, and Supplementary Table 3. By comparing the amount of Ni^{2+}/Ni^{3+} in NCA and NCA-6000 [Figure 4A and B], it is found that the amount of Ni^{2+} increases slightly in the NCA-6000 sample. It may be that the amount of Li^+ in the Li layer is slightly reduced during the heat drive process (500 °C), which is consistent with the results of titration. Compared

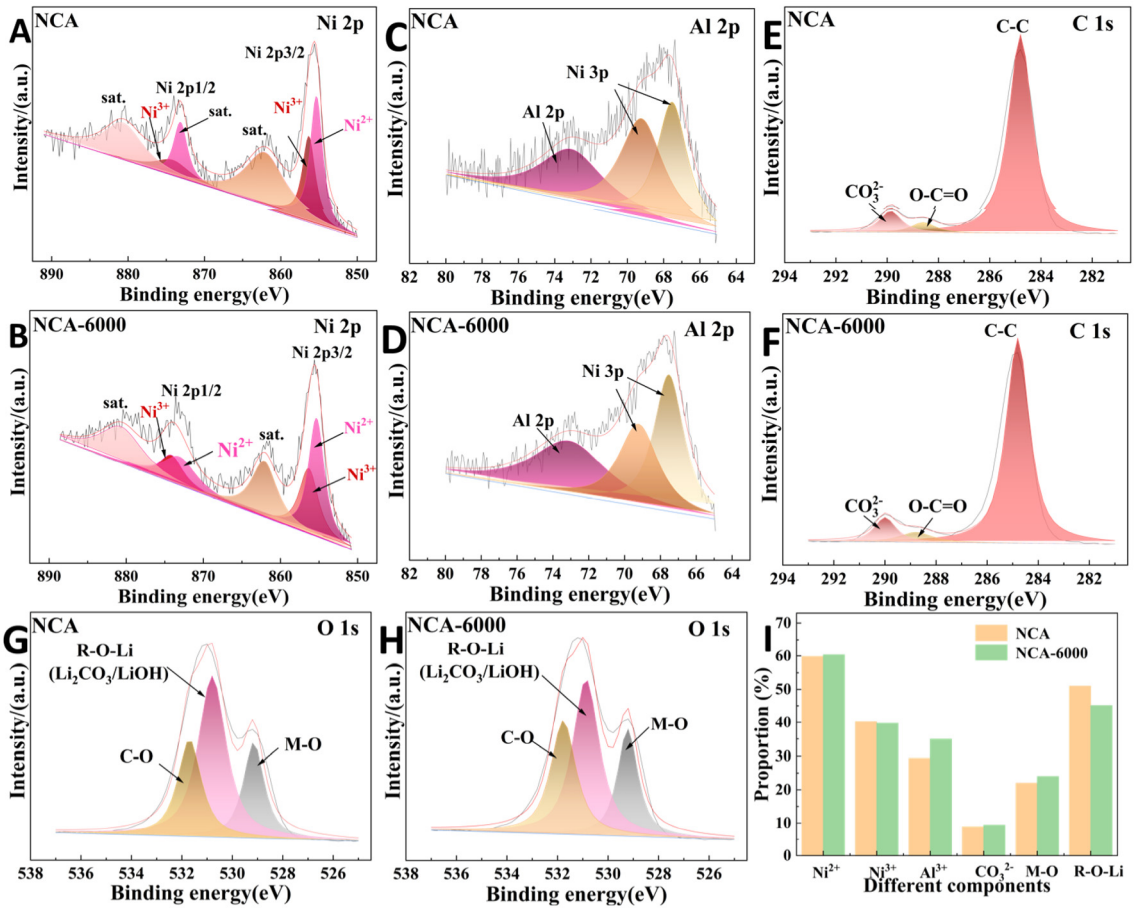

Figure 4. XPS spectra of NCA and NCA-6000 (A and B) Ni 2p; (C and D) Al 2p; (E and F) C 1s; (G and H) O 1 s; (I) the proportion of different components.

with NCA, the Al 2p peak in NCA-6000 also exhibited a slight increase [Figure 4C and D], which can primarily be attributed to the addition of Al_2O_3. In the C1s spectrum [Figure 4E and F], the Li_2CO_3 content in NCA-6000 increased slightly compared to NCA (from 8.9% to 9.4%). This increase can be attributed to the diffusion of a small amount of Li from the interior of the cathode material to its surface during reheating at 500 °C, leading to the formation of new Li_2CO_3 on the surface. Figure 4G and H shows the O 1s spectrum, with peaks at 529.00 eV attributed to lattice oxygen (M-O). The peak at 530.35 eV corresponds to residual lithium compounds (R-O-Li, such as Li_2CO_3 and LiOH) on the surface of the cathode material[13,14,44]. Compared with NCA, the M-O content on the surface of NCA-6000 is slightly increased[45]. This increase may be related to the formation of the $LiAlO_2$@NCA heterostructure. Figure 4G and H presents the O 1s spectrum, where the peak at 529.00 eV is assigned to lattice oxygen (M-O). The peak at 530.35 eV is associated with residual lithium compounds (R-O-Li, such as Li_2CO_3 and LiOH)[13,14,44]. In comparison with NCA, the M-O content on the surface of NCA-6000 shows a slight increase[45]. This enhancement could potentially be linked to the formation of the $LiAlO_2$@NCA heterostructure. Additionally, the R-O-Li peak area in NCA-6000 decreased from 51.0% (in NCA) to 45.1%, indicating a reduction in residual lithium compounds, which can be attributed to the conversion of LiOH by the addition of Al_2O_3.

The study provides a comprehensive evaluation of the electrochemical performance of two cathode material samples: NCA and NCA-6000. The primary focus is on understanding the influence of the $LiAlO_2$@NCA

heterostructure, which is formed through a process of quantitative reconstruction. This heterostructure plays a critical role in altering the surface properties of the cathode materials, thereby affecting their overall electrochemical behavior. In terms of specific electrochemical performance metrics, the results reveal that the NCA-6000 sample demonstrates superior characteristics compared to the standard NCA material. For instance, the initial discharge capacity of NCA-6000 is measured at 206.0 $mAh·g^{-1}$, which represents an improvement over the capacity of the NCA sample of 201.9 $mAh·g^{-1}$ [Figure 5 and Supplementary Table 4]. Additionally, the initial coulombic efficiency of NCA-6000 is recorded at 89.4%, surpassing the 88.9% efficiency of the NCA sample. These enhancements suggest that the formation of the $LiAlO_2$@NCA heterostructure effectively mitigates irreversible capacity loss during the initial electrochemical processes.

The rate performance of the two cathode material samples, NCA and NCA-6000, is visually presented in Figure 5B and further detailed in Supplementary Figure 5A. When comparing the two samples, it becomes evident that the NCA-6000 sample demonstrates superior characteristics in terms of discharge capacity and coulombic efficiency. Across all tested rates, the NCA-6000 consistently delivers higher discharge capacities, indicating its ability to maintain a greater energy output even under high current demands. In addition to higher discharge capacities, the NCA-6000 also exhibits more stable coulombic efficiency compared to the standard NCA material. Coulombic efficiency, which measures the ratio of lithium ions extracted during discharge to those inserted during charge, is a key indicator of a battery's overall efficiency and longevity. Specifically, as the rate increased from 0.1 to 2 C, the rate capacity of NCA-6000 showed a more substantial improvement. The enhanced rate performance of the NCA-6000 sample can be attributed to the formation of the $LiAlO_2$@NCA heterostructure. This architecture optimizes the band structure of the initial system, boosts the electronic conductivity of the cathode material, and minimizes electron polarization during charging and discharging, aligning with the computational findings. Figure 5C and Supplementary Figure 5B demonstrate the cycling stability of the samples within a voltage window of 2.8-4.3 V over 200 cycles at a current density of 1 C. Compared with NCA, the NCA-6000 sample exhibited significantly higher discharge capacity, superior capacity retention, and more stable coulombic efficiency. After 200 cycles (1 C), the NCA-6000 sample maintains a capacity of 137.3 $mAh·g^{-1}$, corresponding to a capacity retention of 77.6%. Conversely, the NCA sample shows a significantly lower discharge capacity of 85.5 $mAh·g^{-1}$ after the same number of cycles, with a retention rate of only 53.3%.

It can be seen that $LiAlO_2$@NCA heterostructure can effectively reduce capacity fade and improve the cyclic stability of cathode materials. Moreover, compared with cathode materials optimized using existing surface modification methods, the NCA-6000 sample exhibits competitive electrochemical performance [Supplementary Table 5].

In order to further clarify how the $LiAlO_2$@NCA heterostructure, obtained via quantitative reconstruction, enhances the reversibility and structural stability of the cathode material, a comparison of the dQ/dV evolution for the NCA and NCA-6000 samples is presented from the 1st to the 200th cycle. This analysis is conducted within the voltage range of 2.8-4.3 V at a rate of 1 C, as illustrated in Figure 5D and E. The dQ/dV curves of both the NCA and NCA-6000 samples show characteristic repeated phase transformations[46]. The behavior of the REDOX peaks in NCA samples provides valuable insights into the material's electrochemical performance and structural stability over repeated charge-discharge cycles. As the number of cycles increases, a gradual decline in the intensity of these REDOX peaks is observed, indicating a potential reduction in the active sites available for redox reactions within the material. In addition to the diminishing intensity, the position of the REDOX peaks also undergoes significant shifts with increasing cycle numbers. In contrast, the reduction peak of NCA-6000 only shows a slight decrease after 200 cycles, with the overall shape of the REDOX peaks remaining intact. These observations indicate that NCA-6000

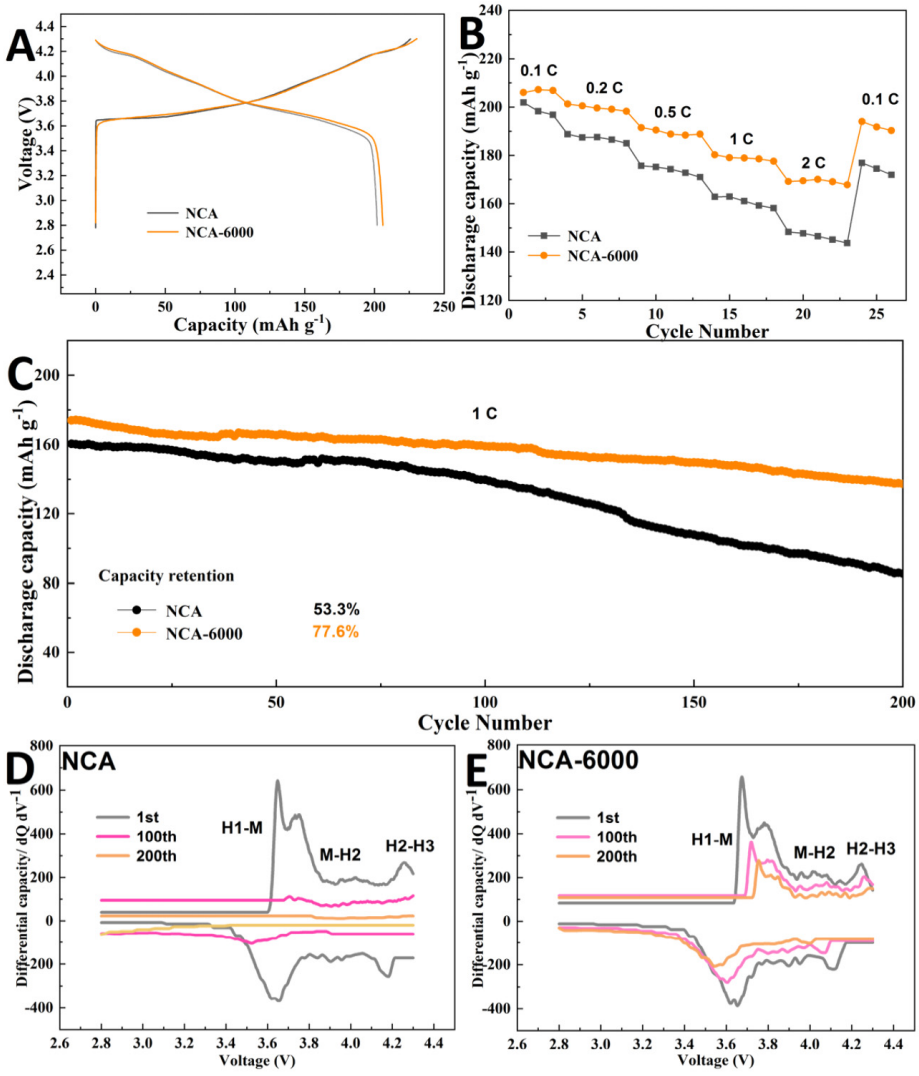

Figure 5. Comparison of electrochemical performances of the sample (A) first charging and discharging profiles; (B) charge-discharge performance at various current densities; (C) Cycling performance at 1 C; dQ/dV curves NCA (D) and Al-4000 (E).

exhibits superior structural reversibility and stability, which is consistent with its excellent cyclic performance demonstrated in Figure 5C.

The outstanding electrochemical performance of cathode materials is strongly linked to the diffusion kinetics of Li^+ and the characteristics of the interfacial environment. To explore in greater detail how the reconstructed $LiAlO_2$@NCA heterostructures influence the dynamics of Li^+ migration, as well as the structural and interfacial stability of cathode materials, analyses are conducted using CV, EIS, and by examining the cross-sections of electrode plates both before and after cycling. As illustrated in Figure 6A-F, CV measurements are performed on NCA and NCA-6000 samples with sweep rates varying from 0.1 to 1.0 $mV{\cdot}s^{-1}$. Both NCA and NCA-6000 samples exhibited distinct repetitive phase transitions. Figure 6A and B illustrates the CV curves of the NCA and NCA-6000 samples at a sweep rate of 0.1 $mV{\cdot}s^{-1}$. After three scans, the voltage drop for the NCA sample is 0.2937 V. In contrast, the voltage drop for the NCA-6000 sample is lower, at 0.2290 V. This indicates that the $LiAlO_2$@NCA heterostructure obtained through quantitative reconstruction provides superior structural reversibility for the cathode material.

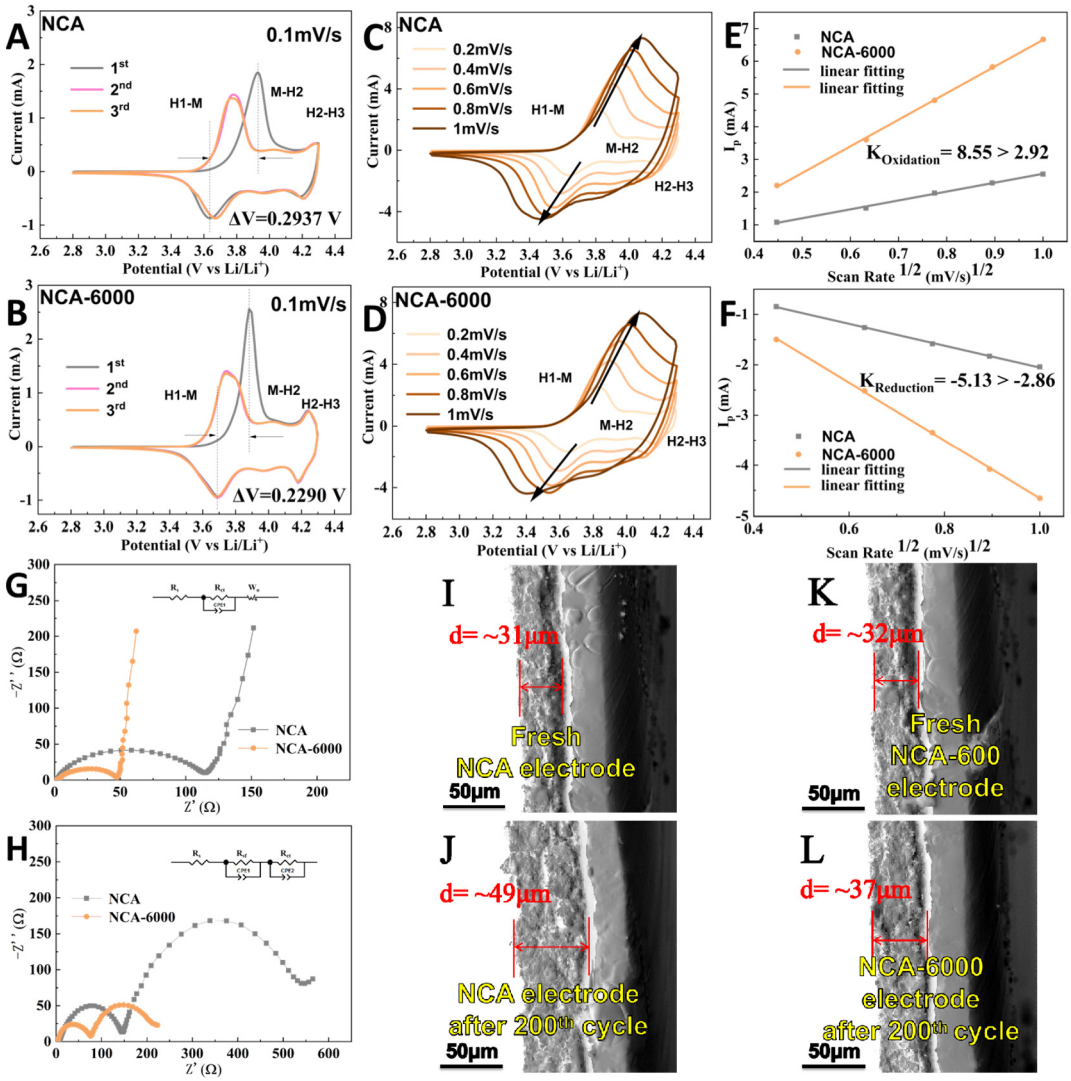

Figure 6. CV curves NCA (A) and NCA-6000 (B) at a sweep speed of 0.1 mV·s^{-1}; CV curves NCA (C) and NCA-6000 (D) at different scanning rates; CV curve comparison (E and F); EIS profiles of NCM and Al-4000 in cycles 0 (G) and 200 (H); (I) The NCA pole plate profile is not tested; (J) NCA pole plate profile after 200 cycles; (K) NCA-6000 pole plate profile is not tested; (L) NCA-6000 pole plate profile after 200 cycles.

Figure 6C and D displays the CV curves acquired at sweep rates varying from 0.2 to 1 mV·s^{-1}. A linear fitting analysis is conducted between the peak REDOX current (I_p) and the square root of the scan rate at various sweep speeds, and the resulting fitting outcomes are shown in Figure 6E and F. It can be observed that the slope (K) of NCA-6000 is greater than that of NCA in both the oxidation and reduction processes. Furthermore, D_{Li} can be determined by employing the Randles-Sevcik equation, as given below[47,48]:

$$I_p = 2.68 \times 10^5 \times n^{3/2} \times A \times D_{Li}^{1/2} \times \upsilon^{1/2} \times C_o \quad (4)$$

$$K = 2.68 \times 10^5 \times n^{3/2} \times A \times D_{Li}^{1/2} \times C_o \quad (5)$$

Here, n refers to the charge number associated with the ion involved in the redox process, which in this case is lithium ions (Li^+), carrying a single positive charge (n = 1). The parameter A denotes the geometric

surface area of the electrode, which is critical for determining the amount of active material participating in the electrochemical reactions. In this context, the electrode surface area is given as 1.33 cm^2. The symbol λ represents the scanning rate used in CV experiments, typically expressed in $mV \cdot s^{-1}$. Lastly, C_o signifies the concentration of lithium ions (Li^+) in the electrolyte solution[47]. Moreover, D_{Li} can be calculated from I_p and the slope K of the curve. According to the fitted curve slopes, the D_{Li} values for the charging processes of NCA and NCA-6000 are 5.89×10^{-9} and 5.18×10^{-8} cm^2S^{-1}, respectively. During the discharging processes, the corresponding the D_{Li} values are 5.89×10^{-9} and 5.18×10^{-8} cm^2S^{-1}, respectively. In both the charging and discharging phases, the NCA-6000 sample demonstrates a significantly higher D_{Li}. These results indicate that the $LiAlO_2$@NCA heterostructure obtained through quantitative reconstruction enhances the Li^+ diffusion kinetics of the cathode material, which is consistent with the excellent magnification performance of NCA-6000.

Excellent electrochemical properties are closely related to the interfacial environment of the material. Therefore, the EIS profiles of NCA and NCA-6000 samples before and after cycling were compared. Figure 6G and H shows the electrochemical impedance spectra of NCA and NCA-6000 samples after the 0th and 200th cycles. Figure 6G presents the equivalent circuit and impedance curve of a battery in its uncharged or discharged state. The curve shows a semicircle in the high-frequency region and a diagonal line in the low-frequency region, indicating R_{ct} and Warburg impedance[49]. The point where the semicircle meets the real axis (Z') at high frequencies corresponds to the ohmic resistance (R_s). This value encompasses the resistance contributed by the electrolyte as well as other resistive components[50]. Figure 6H presents the electrochemical impedance of the battery after 200 cycles at 1 C rate within 2.8-4.3 V. The spectra of cycled cells reveal a high-frequency semicircle linked to the solid electrolyte interface resistance (R_{sf}). This is absent in Figure 6G as the SEI film does not form when uncharged[51]. After cycling, the increase in R_s is primarily attributed to the instability of the electrolyte, leading to increased electrolyte resistance. The results of the fitting are compiled in Supplementary Table 6, demonstrating that the cycled battery has a considerably higher R_{ct} compared to the uncycled battery. Notably, the R_{ct} of NCA-6000 samples was markedly reduced compared to NCA, owing to the enhanced conductivity and reduced interfacial side reactions of NCA-6000. This finding matches the excellent cycling performance of NCA-6000. Results show that the $LiAlO_2$@NCA heterostructure improves cathode conductivity and reduces electrode-electrolyte side reactions through quantitative reconstruction.

The cross-sectional morphology of NCA and NCA-6000 samples before and after cycling was analyzed using SEM. As shown in Figure 6I-L, the thickness of the electrode material on the uncycled NCA and NCA-6000 samples is ~31 and ~32 μm, respectively. It can be observed that the thickness difference between the two samples is minimal when the electrodes are uncycled. SEM is used to analyze the cross-sectional morphology of NCA and NCA-6000 samples before and after cycling. As depicted in Figure 6I-L, the uncycled NCA and NCA-6000 electrode thicknesses are ~31 and ~32 μm, respectively, with minimal difference between them.

However, after 200 cycles, the electrode material on the NCA sample exhibits significant volume expansion, increasing from an initial thickness of ~31 to ~49 μm, which correlates with the low capacity and capacity retention rate observed after 200 cycles. In contrast, after 200 cycles, the electrode material on the NCA-6000 sample shows only a slight volume expansion, from an initial thickness of ~32 to ~37 μm. The reduced volume expansion of the NCA-6000 sample indicates that surface side reactions are effectively suppressed, leading to better interface stability. In conclusion, the $LiAlO_2$@NCA heterostructure obtained through quantitative reconstruction improves electrode interface stability and offers a way to enhance the cycle stability of NCA cathode materials.

CONCLUSIONS

This quantitative reconstruction strategy, which involves adding 6,000 ppm of Al_2O_3 as a Li-reactant to react with the residual 3,156 ppm of LiOH on the NCA surface, not only effectively reduces the residual LiOH and forms a $LiAlO_2$@NCA heterostructure on the NCA cathode material surface but also provides a theoretical basis for the addition of Li-reactants, thereby breaking through the limitations of empirical trial-and-error methods. The developed $LiAlO_2$@NCA heterostructure incorporates interface state features, optimizes the band structure of the initial system, boosts electronic conductivity, decreases the energy barrier for Li^+ migration, and mitigates polarization during charging and discharging. These enhancements collectively lead to improved rate capability and charge-discharge efficiency of the NCA cathode material. Compared to NCA, the NCA-6000 sample exhibits higher discharge capacities at all tested rates. Moreover, the $LiAlO_2$@NCA heterostructure forms a stable protective coating on the NCA cathode surface, reducing unwanted reactions between the electrode and electrolyte, limiting volume changes in the electrode material, improving interfacial stability, and enhancing structural reversibility. These factors collectively improve the cycling stability of the NCA cathode material. Under 1 C conditions, the NCA-6000 sample demonstrated a capacity retention of 77.3% after 200 cycles, which is higher than the 55.3% observed for the NCA sample under identical conditions. The quantitative reconstruction strategy for the surface structure of NCA cathode materials proposed in this study offers a promising approach to developing high-energy-density cathode materials.

DECLARATIONS

Authors' contributions

Provide research ideas, design experimental protocols and writing-original draft: Guo, X.
material preparation, characterization and Electrochemical performance test: Yang, J.; Deng, G.; Cao, X.
Provided technical and material support: Zhang, B.; Deng, T.
review and editing: Zhu, Y.; Liu, J.; Wang, W.
Editing: Xia, S.
All authors revised the manuscript.

Availability of data and materials

All detailed materials and methods supporting the results of this study are included in the article/Supplementary Materials.

Financial support and sponsorship

This work was financially supported by Yunnan Fundamental Research Project (202401AS070001), Yunnan Key Laboratory of Crystalline Porous Organic Functional Materials (202449CE340024), and the Program of Innovative Research Team (in Science and Technology) in the University of Yunnan Province.

Conflicts of interest

Zhu, Y.; Liu, J.; Wang, W. are affiliated with Guizhou Anda Technology Energy Co. Ltd., while all other authors have declared no conflicts of interest.

Ethical approval and consent to participate

Not applicable.

Consent for publication

Not applicable.

REFERENCES

1. Lee, S.; Park, N.; Park, G.; et al. Doping strategy in developing Ni-rich cathodes for high-performance lithium-ion batteries. *ACS. Energy. Lett.* **2024**, *9*, 740-7. DOI
2. Yang, J.; Liang, X.; Ryu, H.; Yoon, C. S.; Sun, Y. Ni-rich layered cathodes for lithium-ion batteries: from challenges to the future. *Energy. Storage. Mater.* **2023**, *63*, 102969. DOI
3. Xia, S.; Cai, Y.; Yao, L.; et al. Nitrogen-rich two-dimensional π-conjugated porous covalent quinazoline polymer for lithium storage. *Energy. Storage. Mater.* **2022**, *50*, 225-33. DOI
4. Xia, S.; Liu, T.; Huang, W.; et al. Extended π-conjugated N-containing heteroaromatic hexacarboxylate organic anode for high performance rechargeable batteries. *J. Energy. Chem.* **2020**, *51*, 303-11. DOI
5. Sagar, R. U. R.; Rahman, M. M.; Cai, Q.; Liang, T.; Chen, Y. I. A comparative study on morphology dependent performance of neodymium - graphene as an anode material in lithium-ion batteries. *J. Energy. Storage.* **2024**, *77*, 109854. DOI
6. Rehman, S. R. U.; Nelson, A.; Fazal, M. W.; et al. An ultralight porous carbon scaffold for anode-free lithium metal batteries. *J. Mater. Chem. A.* **2025**, *13*, 5081-90. DOI
7. Huang, W.; Sun, Y.; Zhao, G.; et al. Constructing nano spinel phase and Li^+ conductive network to enhance the electrochemical stability of ultrahigh-Ni cathode. *Mater. Today.* **2024**, *79*, 86-96. DOI
8. Deng, Z.; Liu, Y.; Wang, L.; et al. Challenges of thermal stability of high-energy layered oxide cathode materials for lithium-ion batteries: a review. *Mater. Today.* **2023**, *69*, 236-61. DOI
9. Wu, Z.; Zhang, C.; Yuan, F.; et al. Ni-rich cathode materials for stable high-energy lithium-ion batteries. *Nano. Energy.* **2024**, *126*, 109620. DOI
10. Ryu, H.; Park, N.; Seo, J. H.; et al. A highly stabilized Ni-rich NCA cathode for high-energy lithium-ion batteries. *Mater. Today.* **2020**, *36*, 73-82. DOI
11. Ryu, H.; Lim, H.; Lee, S. G.; Sun, Y. Near-surface reconstruction in Ni-rich layered cathodes for high-performance lithium-ion batteries. *Nat. Energy.* **2024**, *9*, 47-56. DOI
12. Seong, W. M.; Cho, K. H.; Park, J. W.; et al. Controlling residual lithium in high-nickel (> 90 %) lithium layered oxides for cathodes in lithium-ion batteries. *Angew. Chem. Int. Ed.* **2020**, *59*, 18662-9. DOI
13. Sheng, H.; Meng, X. H.; Xiao, D. D.; et al. An air-stable high-nickel cathode with reinforced electrochemical performance enabled by convertible amorphous Li_2CO_3 modification. *Adv. Mater.* **2022**, *34*, e2108947. DOI
14. Song, M.; Lee, D.; Kim, J.; et al. Chemical decomposition pathway of residual lithium carbonate of Li-ion battery cathodes. *J. Power. Sources.* **2023**, *560*, 232699. DOI
15. Du, Y.; Sheng, H.; Meng, X.; et al. Chemically converting residual lithium to a composite coating layer to enhance the rate capability and stability of single-crystalline Ni-rich cathodes. *Nano. Energy.* **2022**, *94*, 106901. DOI
16. Cao, D.; Tan, C.; Chen, Y. Oxidative decomposition mechanisms of lithium carbonate on carbon substrates in lithium battery chemistries. *Nat. Commun.* **2022**, *13*, 4908. DOI PubMed PMC
17. Cui, Z.; Manthiram, A. Thermal stability and outgassing behaviors of high-nickel cathodes in lithium-ion batteries. *Angew. Chem. Int. Ed.* **2023**, *62*, e202307243. DOI PubMed
18. Seong, W. M.; Kim, Y.; Manthiram, A. Impact of residual lithium on the adoption of high-nickel layered oxide cathodes for lithium-ion batteries. *Chem. Mater.* **2020**, *32*, 9479-89. DOI
19. Freiberg, A. T.; Sicklinger, J.; Solchenbach, S.; Gasteiger, H. A. Li_2CO_3 decomposition in Li-ion batteries induced by the electrochemical oxidation of the electrolyte and of electrolyte impurities. *Electrochim. Acta.* **2020**, *346*, 136271. DOI
20. Cui, Z.; Zuo, P.; Guo, Z.; Wang, C.; Manthiram, A. Formation and detriments of residual alkaline compounds on high-nickel layered oxide cathodes. *Adv. Mater.* **2024**, *36*, e2402420. DOI
21. Wang, C.; Shao, L.; Guo, X.; et al. Air-induced degradation and electrochemical regeneration for the performance of layered Ni-rich cathodes. *ACS. Appl. Mater. Interfaces.* **2019**, *11*, 44036-45. DOI
22. Aktekin, B.; Sedykh, A. E.; Müller-Buschbaum, K.; Henss, A.; Janek, J. The formation of residual lithium compounds on Ni-rich NCM oxides: their impact on the electrochemical performance of sulfide-based ASSBs. *Adv. Funct. Mater.* **2024**, *34*, 2313252. DOI
23. Renfrew, S. E.; McCloskey, B. D. Residual lithium carbonate predominantly accounts for first cycle CO_2 and CO outgassing of Li-stoichiometric and Li-rich layered transition-metal oxides. *J. Am. Chem. Soc.* **2017**, *139*, 17853-60. DOI PubMed
24. Xia, Y.; Chen, A.; Wang, K.; et al. Industrial modification comparison of Ni-Rich cathode materials towards enhanced surface chemical stability against ambient air for advanced lithium-ion batteries. *Chem. Eng. J.* **2022**, *450*, 138382. DOI
25. Gao, Y.; Jiang, R.; Dai, Z.; et al. Revealing the relationships between washing/recalcination processes and structure performance of Ni-rich layered cathode materials. *ACS. Appl. Energy. Mater.* **2022**, *5*, 15069-77. DOI
26. Zhang, S. S.; Fan, X.; Wang, C. Enhanced electrochemical performance of Ni-rich layered cathode materials by using $LiPF_6$ as a cathode additive. *ChemElectroChem* **2019**, *6*, 1536-41. DOI
27. Kim, J.; Zhang, X.; Zhang, J.; Manthiram, A.; Meng, Y. S.; Xu, W. A review on the stability and surface modification of layered transition-metal oxide cathodes. *Mater. Today.* **2021**, *46*, 155-82. DOI

28. Wen, Z.; Song, Y.; Shi, H.; et al. Improved electrochemical performance of single-crystal nickel-rich cathode by coating with different valence states metal oxides. *J. Energy. Storage.* **2024**, *98*, 113037. DOI
29. Wei, J.; Xiong, H.; Zhang, H.; Li, X.; Liu, Y.; Shi, Z. Enhancement in the electrochemical stability at high voltage of high nickel cathode through constructing ultrathin $LiCoPO_4$ coating. *Appl. Surf. Sci.* **2024**, *659*, 159922. DOI
30. Yang, H.; Gao, R. M.; Zhang, X. D.; et al. Building a self-adaptive protective layer on Ni-rich layered cathodes to enhance the cycle stability of lithium-ion batteries. *Adv. Mater.* **2022**, *34*, e2204835. DOI
31. Kim, S.; Kim, M.; Ku, M.; Park, J.; Lee, J.; Kim, Y. B. Coating robust layers on Ni-rich cathode active materials while suppressing cation mixing for all-solid-state lithium-ion batteries. *ACS. Nano.* **2024**, *18*, 25096-106. DOI
32. Wu, F.; Shi, Q.; Chen, L.; et al. New insights into dry-coating-processed surface engineering enabling structurally and thermally stable high-performance Ni-rich cathode materials for lithium ion batteries. *Chem. Eng. J.* **2023**, *470*, 144045. DOI
33. Chu, Y.; Mu, Y.; Zou, L.; et al. Thermodynamically stable dual-modified LiF&FeF_3 layer empowering Ni-rich cathodes with superior cyclabilities. *Adv. Mater.* **2023**, *35*, e2212308. DOI
34. Xia, S.; Huang, W.; Shen, X.; et al. Rearrangement on surface structures by boride to enhanced cycle stability for $LiNi_{0.80}Co_{0.15}Al_{0.05}O_2$ cathode in lithium ion batteries. *J. Energy. Chem.* **2020**, *45*, 110-8. DOI
35. Negi, R. S.; Yusim, Y.; Pan, R.; et al. A dry-processed Al_2O_3/$LiAlO_2$ coating for stabilizing the cathode/electrolyte interface in high-Ni NCM-based all-solid-state batteries. *Adv. Mater. Inter.* **2022**, *9*, 2101428. DOI
36. Park, H. G.; Min, K.; Park, K. A synergistic effect of Na^+ and Al^{3+} dual doping on electrochemical performance and structural stability of $LiNi_{0.88}Co_{0.08}Mn_{0.04}O_2$ cathodes for Li-ion batteries. *ACS. Appl. Mater. Interfaces.* **2022**, *14*, 5168-76. DOI
37. Yang, Z.; Hu, Q.; Yang, H.; et al. Promoting air stability of Co-Li_2O cathode additive via $LiAlO_2$ coating for lithium-ion batteries. *J. Electroanal. Chem.* **2025**, *983*, 119042. DOI
38. Liang, C.; Cheng, Y.; Lv, C.; et al. Surface oxygen-locked $LiNi_{0.6}Mn_{0.4}O_2$: towards stable cycling at 4.7 V. *Energy. Storage. Mater.* **2025**, *75*, 104087. DOI
39. Sun, Y.; Liu, Z.; Chen, X.; Yang, X.; Xiang, F.; Lu, W. Enhancing the stabilities and electrochemical performances of $LiNi_{0.5}Co_{0.2}Mn_{0.3}O_2$ cathode material by simultaneous $LiAlO_2$ coating and Al doping. *Electrochim. Acta.* **2021**, *376*, 138038. DOI
40. Guo, X.; Li, S.; Dai, S.; Wu, S.; Liu, D.; Yang, G. The intricate roles of Al_2O_3 on the structure and electrochemical performances of $LiNi_{0.5}Co_{0.2}Mn_{0.3}O_2$ cathodematerials. *J. Alloys. Compd.* **2024**, *984*, 173931. DOI
41. Lv, Y.; Huang, S.; Zhang, J.; et al. Antimony doping enabled radially aligned microstructurein $LiNi_{0.91}Co_{0.06}Al_{0.03}O_2$ cathode for high-voltage and low-temperature lithium battery. *Adv. Funct. Mater.* **2024**, *34*, 2312284. DOI
42. Zhou, Y.; Zhang, H.; Wang, Y.; et al. Relieving stress concentration through anion-cation codoping toward highly stable nickel-rich cathode. *ACS. Nano.* **2023**, *17*, 20621-33. DOI
43. Li, L.; Chen, Z.; Zhang, Q.; et al. A hydrolysis-hydrothermal route for the synthesis of ultrathin $LiAlO_2$-inlaid $LiNi_{0.5}Co_{0.2}Mn_{0.3}O_2$ as a high-performance cathode material for lithium ion batteries. *J. Mater. Chem. A.* **2015**, *3*, 894-904. DOI
44. Bichon, M.; Sotta, D.; Dupré, N.; et al. Study of immersion of $LiNi_{0.5}Mn_{0.3}Co_{0.2}O_2$ material in water for aqueous processing of positive electrode for Li-ion batteries. *ACS. Appl. Mater. Interfaces.* **2019**, *11*, 18331-41. DOI
45. Wood, K. N.; Teeter, G. XPS on Li-battery-related compounds: analysis of inorganic SEI phases and a methodology for charge correction. *ACS. Appl. Energy. Mater.* **2018**, *1*, 4493-504. DOI
46. Wu, F.; Dong, J.; Chen, L.; et al. High-voltage and high-safety nickel-rich layered cathode enabled by a self-reconstructive cathode/electrolyte interphase layer. *Energy. Storage. Mater.* **2021**, *41*, 495-504. DOI
47. Wu, F.; Kim, G.; Kuenzel, M.; et al. Elucidating the effect of iron doping on the electrochemical performance of cobalt-free lithium-rich layered cathode materials. *Adv. Energy. Mater.* **2019**, *9*, 1902445. DOI
48. Chen, Z.; Kim, G.; Bresser, D.; et al. $MnPO_4$-coated $Li(Ni_{0.4}Co_{0.2}Mn_{0.4})O_2$ for Lithium(-ion) batteries with outstanding cycling stability and enhanced lithiation kinetics. *Adv. Energy. Mater.* **2018**, *8*, 1801573. DOI
49. Jung, C.; Kim, D.; Eum, D.; et al. New insight into microstructure engineering of Ni-rich layered oxide cathode for high performance lithium ion batteries. *Adv. Funct. Mater.* **2021**, *31*, 2010095. DOI
50. Sun, Y.; Wang, C.; Huang, W.; et al. One-step calcination synthesis of bulk-doped surface-modified Ni-rich cathodes with superlattice for long-cycling Li-ion batteries. *Angew. Chem. Int. Ed.* **2023**, *62*, e202300962. DOI
51. Lv, Y.; Huang, S.; Lu, S.; et al. Engineering of cobalt-free Ni-rich cathode material by dual-element modification to enable 4.5 V-class high-energy-density lithium-ion batteries. *Chem. Eng. J.* **2023**, *455*, 140652. DOI